Directed Magnetic Particle Transport above Artificial Magnetic Domains Due to Dynamic Magnetic Potential Energy Landscape Transformation

Dennis Holzinger,* Iris Koch, Stefan Burgard, and Arno Ehresmann

Institute of Physics and Centre for Interdisciplinary Nanostructure Science and Technology (CINSaT),University of Kassel, Heinrich-Plett-Strasse 40, D-34132 Kassel, Germany

ABSTRACT An approach for a remotely controllable transport of magnetic micro- and/or nanoparticles above a topographically flat exchange-bias (EB) thin film system, magnetically patterned into parallel stripe domains, is presented where the particle manipulation is achieved by sub-mT external magnetic field pulses. Superparamagnetic core—shell particles are moved stepwise by the dynamic transformation of the particles' magnetic potential energy landscape due to the external magnetic field pulses without affecting the magnetic state of the thin film system. The magnetic particle velocity is adjustable in the range of 1—100 μm/s by the design of the substrate's magnetic field landscape (MFL), the particle—substrate distance, and the magnitude of the applied external magnetic field pulses. The agglomeration of magnetic particles is avoided by the intrinsic magnetostatic repulsion of particles due to the parallel alignment of the particles' magnetic moments perpendicular to the transport direction and parallel to the surface normal of the substrate during the particle motion. The transport mechanism is modeled by a quantitative theory based on the precise knowledge of the sample's MFL and the particle—substrate distance.

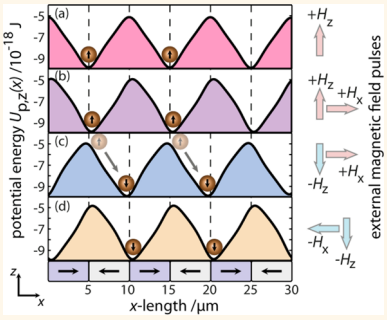

KEYWORDS: particle transport · magnetic bead · exchange bias · IBMP · magnetic field landscape · potential energy landscape

The integration of a remotely controllable magnetic micro- and/or nanoparticle transport into lab-on-a-chip (LOC) systems promises to play a key role for the development of future cost-efficient devices for biological, chemical, medical, and life science applications.[1−4] Because of their inherent material properties, magnetic particles are versatile for a variety of on-chip applications like isolation, separation, and purification of specific biomolecules,[5] the mixing of the smallest liquid volumes,[6−8] or the directed transport[9] of biological cargo[10] to designated chip areas.

The velocity of a magnetic particle relative to the carrier fluid above nonmagnetic substrates and in nonmagnetic environments is determined by the strength of an applied magnetic field, its field gradient, and the flow resistance of the particle.[9,11] The maximum achievable velocity for a given particle in a liquid is therefore restricted by the maximum available external magnetic field $\vec{H}$ and its gradient $\vec{\nabla}\vec{H}$. The use of substrates producing local magnetic fields when combined with an external magnetic field, however, may considerably increase achievable particle velocities, since such local fields, although not too strong, possess very strong field gradients.

For a particle transport by these local fields two main concepts emerged. In the first, particles in solution are captured by the inhomogeneous magnetic fields above domain walls, occurring, for example, in magnetically patterned exchange-bias (EB) layer systems,[9] magnetic garnet films,[12] or ferromagnetic nanowires.[10] Then the particle transport is achieved by the directed motion of the domain walls during the magnetization reversal of the substrate. In the second concept, a spatially periodic magnetic field landscape (MFL) is used, fabricated by periodically arranged local magnetic field sources. The corresponding potential energy landscape for a magnetic particle is periodically modified by a

* Address correspondence to holzinger@uni-kassel.de.

Received for review April 16, 2015 and accepted July 2, 2015.

Published online July 02, 2015
10.1021/acsnano.5b02283

superposition of the substrate's MFL with an external magnetic field changing with frequency ω_{ext}. In this concept, the sample's magnetic state is not affected.[13,14] The spatial change of the potential energy landscape determines the force $\vec{F}_M = -\vec{\nabla}U_M$ on the particles and thus their velocities.[11] Consequently, the particles will follow the laterally shifting potential energy minimum as long as ω_{ext} does not exceed a critical value ω_c, at which the particles cannot follow the shift of the potential energy minimum anymore.[13] As in this concept no magnetization reversal of the substrate is necessary, it is particularly promising for battery powered portable LOC devices, since small external magnetic fields are already sufficient for the performance of the particle transport.

In the present contribution, we will show that the magnetically stripe patterned EB layer system used for the transport of superparamagnetic core−shell particles by moving domain walls,[9] can be also used for a particle transport when only very small homogeneous external magnetic fields are applied, that is, when its magnetization state is not changed. The particle transport process will be quantitatively modeled for a sequence of designed homogeneous external magnetic fields pulses for a particle−substrate distance range where the substrate's MFL is quantitatively available.[15] The theoretically predicted particle velocity will be tested by corresponding quantitative experiments. The difference between the particle velocity and the velocity of the potential energy minimum in combination with the width of the artificial parallel stripe domains determine the threshold frequency of the external magnetic field pulses above which no directed particle motion occurs.

THEORETICAL MODEL

The potential energy $U_P(x,z)$ of a superparamagnetic core−shell particle with magnetic moment $\vec{m}_P(x,z)$ in a magnetic field $\vec{H}(x,z)$ at its lateral position x and at z above the substrate is given by the inner product[16]

$$U_P(x,z) = -\mu_0 \vec{m}_P(x,z)\cdot\vec{H}(x,z) \quad (1)$$

where μ_0 is the vacuum permeability. Owing to the parallel stripes in the y-direction the potential energy is independent of the y-coordinate (Figure 1). The magnetic moment $\vec{m}_P$ of the superparamagnetic particles as a function of a magnetic field and its direction relative to the surface normal vector (angle $\alpha = \tan^{-1}[H_z(x,z)/H_x(x,z)]$) is described in point particle approximation by the Langevin function[17]

$$|\vec{m}_P(x,z)| = m_S[\coth(b\cdot|\vec{H}(x,z)|) - (1/(b\cdot|\vec{H}(x,z)|))] \quad (2a)$$

$$m_{P,x}(x,z) = \cos(\alpha)\cdot|\vec{m}_P(x,z)|,$$
$$m_{P,z}(x,z) = \sin(\alpha)\cdot|\vec{m}_P(x,z)| \quad (2b)$$

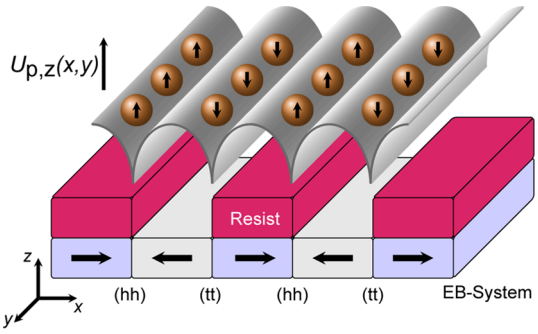

Figure 1. Sketch of the artificial magnetic domain pattern of the substrate's magnetic layer system and the coordinate system used throughout the text. The magnetic substrate is a topographically flat exchange-bias (EB) thin film system, magnetically patterned into parallel stripe domains with head-to-head (hh) and tail-to-tail (tt) orientation of the magnetization in adjacent domains. The photoresist pattern was used to fabricate the artificial magnetic domain structure during the ion bombardment induced magnetic patterning (IBMP) procedure and kept as a spacer for some of the transport experiments (thickness not to scale with thickness of magnetic layer system and width of the domains). The particles' magnetic potential energy landscape $U_{p,z}(x,y)$ in the absence of an external magnetic field is sketched for a fixed particle to substrate distance.

with the saturation magnetic moment m_S, the Boltzmann constant k_B, the temperature T, and the Langevin parameter $b = m_s\mu_0/(k_BT)$. In the absence of an external magnetic field, the particle's magnetic moment is solely influenced by its position within the substrate's MFL. Hence, the precise determination of the MFL is crucial to adequately describe the magnetic forces acting on the particles.[13] Recently, the magnetic field landscape as a function of position was experimentally determined by μ-Hall probe measurements within a height range between 0.75 and 2.65 μm over the sample surface.[15] It was shown there, that the MFL in this height range can be reasonably well described by an analytical model which will be also employed here. The model is based on the description of the change of magnetization when passing from one domain to the other over a domain wall by the empirical function[18]

$$M_x(x) = \pm(2M_r/\pi)\tan^{-1}(x/a) \quad (3)$$

which was originally developed for a pure ferromagnetic layer in longitudinal recording media. In eq 3, M_r is the remanent magnetization of the ferromagnetic layer and a is the domain transition parameter related to the domain wall transition length l_W *via* $l_W = \pi\cdot a$.[18]

Several parallel magnetic stripe domains and their magnetization transitions are described by a finite sequence of domain transitions individually displaced by the stripe widths and with alternating sign, depending on whether the transition is of head-to-head (hh) or tail-to-tail (tt) type (Figure 1). The magnetic field

distribution $\vec{H}_{MFL}(x,z)$ over one transition can be analytically described by[15,19]

$$H_{x,MFL}(x,z) = 4M_r\left[\tan^{-1}\left(\frac{x(d_F+z)}{x^2+a^2+a(d_F+z)}\right) - \tan^{-1}\left(\frac{xz}{x^2+a^2+az}\right)\right] \quad (4a)$$

$$H_{z,MFL}(x,z) = 2M_r \log\left(\frac{x^2+(d_F+z+a)^2}{x^2+(z+a)^2}\right) \quad (4b)$$

where d_F is the thickness of the ferromagnetic layer. The quantitative determination of the MFL *via* μ-Hall measurements revealed the magnitude of the magnetic field as a function of the z-distance above the sample surface ($H_z(z)$) at an x-position in the center of the domain wall.[15] The observed data was fitted by eq 4b, where a and M_r were chosen as free fit parameters. The domain transition parameter was determined to $a \approx 150$ nm, corresponding to a domain transition length of $l_W \approx 450$ nm,[15] the fit parameter for the remanent magnetization was $M_r = 41$ kA/m according to the $Co_{70}Fe_{30}$ layer thickness of 6.5 nm. The H_z component of the MFL exponentially decays with increasing distance to the substrate surface, where the $H_{z,MFL}/e$ decay is present at a distance of z = 300 nm above the sample surface for the here described MFL. The particle's magnetic moment and the corresponding potential energy landscape can now be calculated according to eq 1 and 2, taking into account the effective magnetic field $\vec{H}_{eff}(x,z,t)$ which is a superposition of $\vec{H}_{MFL}(x,z)$ and the homogeneous external magnetic field $\vec{H}_{ex}(x,z,t)$. The magnetic force $\vec{F}_M$ acting on a magnetic particle at position x,z at time t is then determined by[1,16]

$$\vec{F}_M(x,z,t) = -\vec{\nabla}U_P(x,z,t) = -\mu_0(\vec{m}_P(x,z,t)\cdot\vec{\nabla})\cdot\vec{H}_{eff}(x,z,t) \quad (5)$$

where the second part of eq 5 holds for a point dipole.

In a liquid environment, the steady-state particle velocity $\vec{v}_P$ will be reached when the magnetic force $\vec{F}_M$ (eq 5) balances the drag force $\vec{F}_D$. Here, the time interval for the particle acceleration will be neglected since this time is about 1 μs for the present particle/liquid system, which is much smaller than all relevant time intervals of the present experiments. The drag force can be described by the Stokes law for low Reynolds number laminar flow, which is a good approximation for the present microfluidic device[20]

$$\vec{F}_D(x,z) = 3\cdot\pi\cdot d_P\cdot\eta_L\cdot f_D(z)\cdot\vec{v}_P(x,z) \quad (6)$$

where η_L is the viscosity of the fluid and f_D is the drag force coefficient which depends on both the particle diameter d_P and the particle-substrate distance. For a particle moving close or onto the substrate the drag coefficient is maximal; that is $f_{D,max} \approx 3$, whereas for a particle moving far away from the substrate surface $f_D = 1$. Note that f_D exponentially decays from the substrate surface into the liquid.[20] For the here described particle liquid system with $d_p = 2$ μm, the drag coefficient is $f_{D,max}/2 = 1.5$ (half of the maximum) at a particle–substrate distance of 70 nm. According to eq 5 and 6 the spatial distribution of the particle velocity in the plateau of the external magnetic field writes as

$$\vec{v}_P(x,z) = -\frac{\mu_0(\vec{m}_P(x,z)\cdot\vec{\nabla})\cdot\vec{H}_{eff}(x,z)}{3\cdot\pi\cdot d_P\cdot\eta_L\cdot f_D(z)} \quad (7)$$

Clearly, the steady-state particle velocity is dramatically influenced by the magnitude and gradient of the effective local magnetic field. High magnetic fields possessing large field gradients over small distances can therefore be used to obtain high steady-state velocities, even at small absolute magnitudes of the external magnetic field. Such gradients can be designed in a controlled fashion for the here presented EB layer system possessing artificial magnetic domains.[21] Besides, the particle–substrate distance is an important issue concerning the particle's steady-state velocity. The decreasing drag force coefficient with increasing z-distance to the substrate would result in an increase of the particle velocity. At the same time the local magnetic fields and its gradients decrease with increasing z-distance, therefore reducing the particle velocity. These two effects with opposite trends lead to a certain height above the substrate, at which the particle velocity is maximum.

For the numerical simulations of the samples' MFL a sequence of 10 domain transitions according to 10 domain walls is implemented into the analytical model of eq 4 by using a rectangular mesh of dimensions x = 50 μm and z = 5 μm with a regular element size of 10 × 10 nm^2 (xz-plane). The particle's magnetic potential energy landscape at different external magnetic field values is calculated according to the effective magnetic field dependence of the particle's magnetic moment (eq 1 and 2). The particle diameter, the particle's saturation magnetic moment and the Langevin parameter at room temperature are chosen with respect to the experimental conditions; that is, $d_P = 2$ μm, $m_S = 4.48 \times 10^{-14}$ Am^2 and $b = 1.4 \times 10^{-4}$ 1/m. The viscosity of the fluid is set to be $\eta_L = 1.002 \times 10^{-3}$ Pa·s according to the material properties of water at room temperature. Since local fluctuations of both the EB substrate's MFL magnitude and gradient can occur because of the sample fabrication procedure process, the resulting deviations will be taken into account for the calculation of the steady-state particle velocity. The error estimate is performed by changing the magnitude of the remanent magnetization M_r of the $Co_{30}Fe_{70}$ layer (linear scale) related to a change of the $Co_{30}Fe_{70}$ layer thickness in the interval of d_F = 6.5 ± 0.5 nm; that is, M_r = 38 kA/m (d_F = 6 nm) and M_r = 44 kA/m

(d_F = 7 nm). According to eq 4a and 4b, both the magnitude and gradient of the MFL are changed when M_r and d_F of the ferromagnetic layer are altered.

RESULTS AND DISCUSSION

The transport experiments were performed by applying trapezoidal external magnetic field pulses in the *x*-and *z*-directions. During the experiments, particles were kept in a defined height range above the substrate surface where measurements of the EB substrate's MFL are available and the analytical model can be used to quantitatively describe the MFL.[15] For a proof-of-principle experiment, the 700 nm high resist structure was preserved (Figure 1). As the particles pass the 5 μm wide gaps at an average time of 125 ms, the distance they are falling by the combined action of gravity and buoyancy while traversing the gaps of the resist structure was estimated to be Δz = 25 nm. Since this is negligible compared to the particle diameter of 2 μm, the particles will stay on top of the resist structure, ensuring a minimum particle-surface to substrate distance of 700 nm for particles moving over the trenches of the resist structure where $f_D \approx 1$ (minimum distance between particle-center and substrate surface of 1.7 μm). For a systematic investigation of the particle velocity, experiments were performed by first removing the resist stripes with 3% KOH solution and acetone, and subsequently recoating the sample with a 700 nm thick AZ1505 layer without topographic modulations; that is, $f_D \approx 3$ for a particle moving close to the resist surface.

In the absence of the external magnetic field, the particles are attracted by the EB substrate's inhomogeneous magnetic fields arising above the hh and tt domain walls between the oppositely magnetized magnetic domains (Figure 1). The superparamagnetic core−shell particles equally distribute themselves above the hh and tt walls, since the two involved magnetic potential energies are almost degenerate.[9] Therefore, an initial arrangement of particle rows at regular distances of 5 μm is observed, corresponding to half the periodicity of the artificial magnetic domain pattern of the EB system (Figure 1). Because of the parallel alignment of the particles' magnetic moments in one row (along the *y*-direction) above the same domain wall (Figure 1), the particles repel each other magnetostatically. For the present particle type repulsive forces of ≥10 nN at interparticle distances ≤1 μm are obtained. Therefore, particle clustering is largely avoided.

The particle transport proceeds through the dynamic transformation of the particles' magnetic potential energy landscape in the presence of both the EB substrate's MFL and the trapezoidal external magnetic field pulses $H_x(t)$ and $H_z(t)$, where $H_x(t)$ is phase-shifted by a quarter cycle duration with respect to $H_z(t)$ (Figure 2). In the present experiments, the rise and fall time intervals of the trapezoidal magnetic field pulses are rather short due to the high magnetic field alteration rate of $v_H = 3.2 \times 10^6$ (A/(m·s)) for both $H_x(t)$ and $H_z(t)$. Hence, the particles may move a maximum distance of 20 nm during the longest pulse rise time interval of 0.5 ms for H_z with the highest observed average particle velocity of about 40 μm/s. Since this distance is negligible in comparison to the particle diameter of 2 μm, the following discussion of the particle transport steps refers to the plateau times of $H_x(t)$ and $H_z(t)$, where $H_x = \pm H_{x,max}$ and $H_z = \pm H_{z,max}$.

Numerical calculations of the particles' magnetic potential energy landscapes at a particle-center to EB substrate distance of 2 μm for different external magnetic field pulse configurations $H_x = \pm H_{x,max} = \pm$ 320 A/m and $H_z = \pm H_{z,max} = \pm$ 1640 A/m based on the above-described theoretical model are shown in Figure 2a−e. During $0 < t \leq T/4$ (cycle duration T), only the *z*-component of the external magnetic field $H_z(t) = \pm H_{z,max}$ is superimposed on the EB substrate's MFL since $H_x(t) = 0$ (Figure 2f). As a result of the superposition of the oppositely directed H_z components of the EB substrate's hh and tt domain walls and the external magnetic field pulse $H_z(t) = +H_{z,max}$, the particles' magnetic potential energies above the two domain wall types are no longer energetically degenerate (see Figure 1 and Figure 2a). Hence, the effective magnetic field above the hh domain walls is stronger than the effective magnetic field above the tt domain walls. Consequently, particles initially located above the tt domain walls will statistically move either in +*x*- or in −*x*-direction into the nearest potential energy minima above the hh domain walls at their steady-state velocity induced by the spatial gradient of the magnetic potential energy landscape (Figure 2a). After this first undirected transport step, all particles are now located above the hh domain walls, that is, the same domain wall type, which enables a simultaneous manipulation of all particles in the following steps. In addition, the distance between the particle rows (particle-center to particle-center) is increased from 5 to 10 μm, that is, twice the magnetic domain width of the magnetically stripe patterned EB thin film substrate.

For $t > T/4$, both $H_x = \pm H_{x,max}$ and $H_z = \pm H_{z,max}$ are present (Figure 2f), and hence four different pulse configurations can be distinguished within one cycle duration of the external magnetic field sequence: (1) $+H_{x,max}$, $+H_{z,max}$, (2) $+H_{x,max}$, $-H_{z,max}$, (3) $-H_{x,max}$, $-H_{z,max}$ and (4) $-H_{x,max}$, $+H_{z,max}$ (Figure 2b−e). The superposition of both $H_{x,max}$ and $H_{z,max}$ and the EB substrate's MFL causes a slight shift of the magnetic potential energy minima to smaller or larger *x*-coordinates with respect to the hh or tt domain wall centers in dependence on the sign of both $H_{x,max}$ and $H_{z,max}$ (Figure 2b−e). Furthermore, the particles' magnetic moment is slightly tilted from the *z*-axis due to

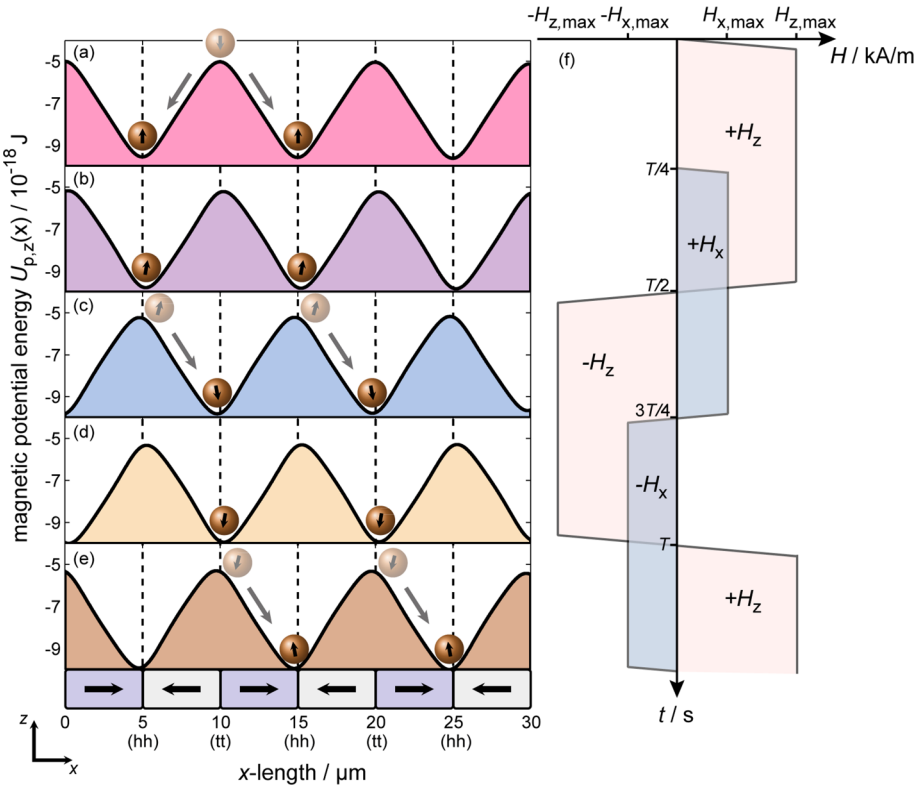

Figure 2. (a–e) Calculated magnetic potential energy landscape $U_{p,z}(x)$ as a function of the *x*-coordinate (parallel to the EB-systems short stripe axis) at a particle-center to substrate distance of 2 μm for different external magnetic field configurations of $H_x = \pm H_{x,max}$ and $H_z = \pm H_{z,max}$ (f). The two particles are exemplarily added to visualize the particle transport during the applied external magnetic field pulse configurations and the corresponding transformation of the particles magnetic potential energy landscape. Note that the transport scheme from panels b to e is repeated until the external magnetic field sequence stops. The magnetic particle rows are essentially transported between two neighboring domain walls when the field direction of $H_{z,max}$ is reversed, whereas a slight shift of the potential energy minima to smaller or larger *x*-coordinates with respect to the domain wall center occurs, when the sign of $H_{x,max}$ is changed.

the *x*-component of the effective magnetic field acting on the magnetic particles (Figure 2b–e).

The directed transport of magnetic particles between two neighboring domain walls is induced by a change of the field direction of $H_{z,max}$, while the direction of $H_{x,max}$ remains constant, that is, a transition between the external magnetic pulse configurations (1) and (2) (Figure 2b, c) or (3) and (4) (Figure 2d, e), respectively. When the field direction of $H_{z,max}$ is reversed, for example, from $+H_{z,max}$ to $-H_{z,max}$ (pulse configurations (1) and (2)), the negative H_z-component of the external magnetic field now increases (decreases) the effective magnetic field above the tt domain walls (hh domain walls). The potential energy minima above the hh domain walls are accordingly transformed into maxima of the potential energy landscape. Note that the displacement of the magnetic potential energy minimum, which proceeds at an average velocity of v_U = 10 mm/s according to the external magnetic field alteration rate v_H, is again much faster than the experimentally observed maximum steady-state velocity of the moving particles. Therefore, the particle rows will move into the direction of the closer potential energy minimum, in the present case along the $+x$-direction, at their steady-state velocity induced by the spatial gradient of the magnetic potential energy landscape. The magnetic potential energy landscape responsible for the directed motion of particles hence always corresponds to the external magnetic field pulse configuration after the switching of $H_{z,max}$, as indicated in Figure 2c and e, respectively.

The particle movement direction in this concept is prescribed by the sign of $H_{x,max}$ during the switching of $H_{z,max}$ since the potential energy minima are either shifted to smaller or larger *x*-coordinates with respect to the domain wall center (hh or tt) prior to the transport step. For the present experiments, the potential energy minima are shifted by $\pm$200 nm with respect to the domain wall center in the relevant particle–substrate range depending on both the sign of $H_{x,max}$ (Figure 2b–e) and the domain wall type. The theoretical distance the particles are transported during one transport step is therefore reduced by a factor of 2 times the potential energy minimum shift with respect to the domain wall center, that is, by 400 nm from 5 to 4.6 μm.

The particle rows are essentially moving with their steady-state velocity at the plateau times where $H_z = \pm H_{z,max}$. Therefore, the transport will work as long

as the time the particles need to travel from one domain wall to the next is shorter or equal to the plateau time of the external magnetic field pulse $\pm H_{z,max}$. Within the H_z plateau times the particle velocity is strongly influenced by the magnitude and gradient of the samples' MFL, the magnitude and gradient of the external magnetic field H_z, and the actual particle−substrate distance. For a fixed external magnetic field alteration rate, the particle velocity should be independent of the frequency ω_{ext} of the external magnetic field. This hypothesis was experimentally investigated by determining the steady-state particle velocity as a function of ω_{ext} (Figure 3). Obviously, the experimentally determined average particle velocity $\overline{v}_P$ observed at different frequencies ω_{ext} of $\overline{v}_P = 36 \pm 4\ \mu$m/s is almost independent of ω_{ext} (Figure 3). For $\omega_{ext} > \omega_c \approx 16$ Hz, no particle transport was observed. From $\overline{v}_P = 36 \pm 4\ \mu$m/s, the average time for a single transport step of approximately 5 μm length (depending on the size of the slight shift of the energy minima before and after the transport step) is about $\Delta = 150 \pm 50$ ms, which corresponds to half the time interval of the critical cycle duration $T_c \approx 400$ ms or the plateau time Δt_p. Hence, if the potential energy minimum starts to move again before the particles have reached their final position close to the domain wall center, the phase correlation between the movement of the particles and the potential energy minimum breaks down. As a result, the particles start to oscillate around the domain wall center due to the oppositely directed forces induced by the high frequency switching of the particles' potential energy landscape.

The experimental data of the particle movement was compared to the theoretically predicted particle velocities according to eq 1−7. These velocities were obtained by numerical simulations of the magnetic potential energy landscape at different particle−substrate distances above the 700 nm resist layer according to the numerical scheme presented in the theoretical model. The uncertainty of the simulated particle velocity was estimated by changing the magnitude and gradient of the samples' MFL (see explanation in the Theoretical Model section), where the obtained particle velocities of $v_{P,sim,min}$ and $v_{P,sim,max}$ correspond to a theoretical $Co_{30}Fe_{70}$ layer thickness of 6 and 7 nm, respectively. The calculation of $v_{P,sim,min}$ and $v_{P,sim,max}$ therefore takes into account local fluctuations of the MFL's magnitude and gradient, for example, due to the sample fabrication procedure process. In the simulations, the particles' steady-state velocity $v_{P,sim}$ first exponentially increases with increasing particle−resist distance (surface to surface distance) due to the more rapid decrease of f_D in comparison to $H_{z,MFL}$ with respect to the particle−resist distance (see Figure 4). The particle velocity is a maximum at a particle−resist distance of 320 nm for

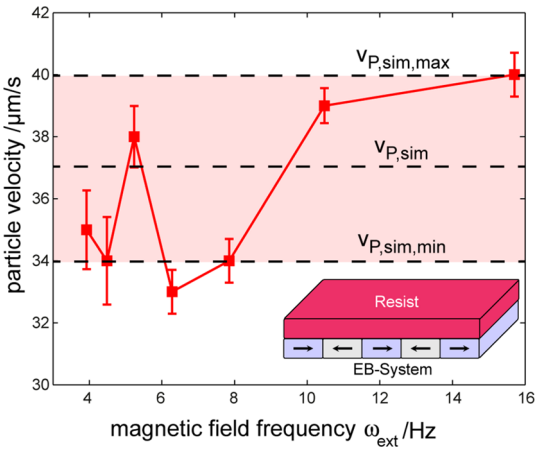

Figure 3. Experimentally obtained particle velocity as a function of the applied external magnetic field frequency ω_{ext}. For these experiments, the sample was recoated with 700 nm photoresist without topographic modulations as shown in the inset. The theoretically predicted particle velocity $v_{P,sim}$ was obtained at a particle-resist distance of 320 nm. The uncertainty of $v_{P,sim}$ in terms of $v_{P,sim,min}$ and $v_{P,sim,max}$ was estimated by changing the $Co_{30}Fe_{70}$ layer thickness to $d_F = 6.5 \pm 0.5$ nm and therefore the sample's MFL. Above the critical frequency of $\omega_{ext} \approx 16$ Hz no particle transport is observed.

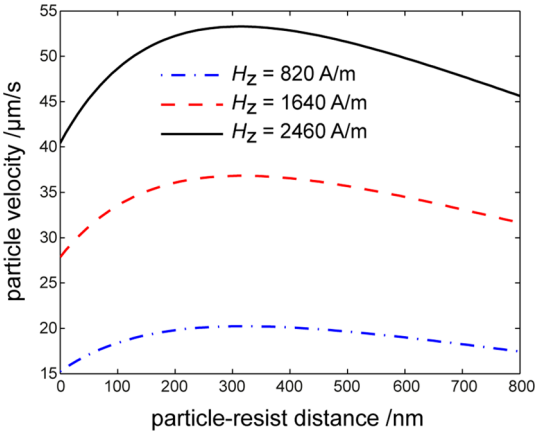

Figure 4. Theoretically predicted particle velocity as a function of the particle−resist distance (surface to surface distance) shown for different values of H_z at a fixed H_x field of $H_x = 320$ A/m. Since the spatial gradient of the effective magnetic field is not affected by the application of a homogeneous external magnetic field pulse, the particle−resist distance of about 320 nm at which the particle velocity is maximum remains almost the same.

the here applied maximum external magnetic field pulses of $H_x = \pm 320$ A/m and $H_z = \pm 1640$ A/m, corresponding to an overall particle-surface to substrate distance of 1020 nm. By further increasing the particle−resist distance the particle velocity exponentially decreases. Since in the experiments the moving particles are obviously not sticking to the resist surface, we assume that particles will move with their theoretically predicted maximum particle velocities at a particle−resist distance of 320 nm (Figure 4). As can be seen from Figure 3, the theoretical average steady-state particle velocity of $v_{P,sim} = 37 \pm 3\ \mu$m/s at a

particle−resist distance of 320 nm is in good agreement to the experimentally observed data. According to Figure 4, the simulations predict a further increase (decrease) of the particle velocity by increasing (decreasing) the magnitude of the applied external magnetic field pulse H_z while H_x is fixed. Since the spatial gradient of the effective magnetic field landscape is only affected by the application of inhomogeneous external magnetic field pulses, the particle−substrate distance at which the particle velocity is maximum remains almost the same when increasing (decreasing) the magnitude of the homogeneous external magnetic field pulse H_z (Figure 4).

Note that the particle's magnetic potential energy in the above-described model is always calculated to be about 3 orders of magnitude larger than the thermal energy present at room temperature and therefore dominates over the stochastic thermal motion. In contrast to the earlier introduced models of traveling wave magnetophoresis,[13,14] the here-presented particle transport concept is strongly influenced by the spatial distribution of the sample's MFL, which for the current layer system can be tailored to a large degree. In addition, the described particle transport concept was experimentally tested to work for long operation times exceeding 1 h without further modification of the substrate's surface, which might be particularly promising for the application of this technique into bioassays in LOC devices.

CONCLUSION

In summary, we have presented a novel concept for the directed transport of full superparamagnetic particle rows employing very weak external magnetic field pulses. A quantitative model for the transport was developed and compared to experiment, transporting particles with 2 μm diameter at a minimum substrate to particle-surface distance of 700 nm over a magnetic parallel stripe patterned EB layer system covered by a resist layer. It was shown that the particles move at their steady-state velocities during the plateau time intervals of the trapezoidal external magnetic field pulse sequences. This finding can be used to modify the transport velocity of the particles by either artificially changing the particle-substrate distance *via* resist covering of the EB substrate or by the specific design of the MFL above the magnetically patterned EB layer system during the IBMP fabrication procedure.[21] In comparison to other techniques based on nonmagnetic substrates and large external magnetic gradient fields, this technique offers many advantages: (1) the particles are moving in a controlled manner at regular interparticle distances close to the substrate and are not randomly distributed within the liquid; (2) the inherent magnetostatic repulsion between the particles largely avoids particle agglomeration whereas particle agglomeration largely occurs on substrates without MFLs; (3) the particle velocity can be specifically tailored by the intrinsic material properties of the EB layer system without topographical modulations of the substrate. Hence, the sample manufacturing effort seems to be small in comparison to the gain of the adjustment possibilities, particularly under the aspect of a high throughput sample fabrication. Furthermore, the simulations demonstrate that the particle velocity can be additionally modified by altering the magnitude of the external magnetic field pulses.

The directed particle transport only works if the frequency of the external magnetic field sequence is smaller than a certain critical frequency ω_{ext} at which the switching of the particles' magnetic potential energy landscape is faster than the time the particles need to travel for approximately one domain width into the nearest potential energy minimum. The latter characteristic opens up a wide field of magnetophoretic applications since particles with different magnetophoretic mobilities can be easily separated when raising the external magnetic field alteration above the critical frequency of one particle type.[10,14] In this sense, this technique might be used in order to first purify and subsequently concentrate low-concentrated biomolecules from solution for further on-chip quantification procedures. If the sample's MFL is interfering at a later stage in the application, the sample can be uniformly magnetized by applying an external magnetic field above the EB field of the sample and hence, the sample's MFL is suppressed. The possibility to perform the presented particle transport in longtime experiments at small external magnetic field strengths of only a few mT gives further rise for the integration of this technique into low-cost portable LOC applications.

EXPERIMENTAL SECTION

The bottom of the microfluidic chamber consisted of an EB layer system with artificial parallel stripe magnetic domains with head-to-head (hh) and tail-to-tail (tt) magnetization orientations in adjacent domains (Figure 1). The EB layer system was $Cu^{50\ nm}/Ir_{17}Mn_{83}{}^{10\ nm}/Co_{70}Fe_{30}{}^{6.5\ nm}/Ta^{10\ nm}$, grown by dc magnetron sputter deposition on a naturally oxidized Si(100) substrate in an applied magnetic field of 3 kA/m at room temperature (RT). Subsequently, the unidirectional anisotropy was set by field cooling in an applied magnetic field of 80 kA/m parallel to the uniaxial anisotropy axis of the ferromagnetic layer. The system was first heated to 573 K for 1 h and then cooled to RT at a cooling rate of $f_C = -4$ K/min. From vibrating sample magnetometry (VSM) hysteresis loop measurements the sample's average initial EB-field was determined to be $|\vec{H}_{EB,0}| = 33 \pm 1$ kA/m with an average coercive field of $H_{C,0} = 7 \pm 1$ kA/m. The artificial parallel stripe domains with their long stripe axes $\vec{l}$ perpendicular to $\vec{H}_{EB,0}$, were fabricated by ion bombardment induced magnetic patterning (IBMP)[22−29] using a home-built Penning ion source.[30] Briefly, a 700 nm thick

photoresist (AZ1505, purchased at Microchemicals) parallel stripe structure with a stripe width of 5 μm and a periodicity of 10 μm was prepared as a shadow mask for the ion bombardment on top of the Ta capping layer *via* UV lithography. The average thickness of the photoresist was determined *via* AFM measurements and was chosen to prevent 10 keV He^+ ion penetration into the magnetic layer system. He-ion bombardment was performed with an ion fluence of $J_{IB} = 5 \times 10^{15}$ ions/cm^2 in an applied in-plane magnetic field of 80 kA/m antiparallel to $\vec{H}_{EB,0}$, hence, creating magnetic parallel stripe domains with hh and tt orientation of the remanent magnetizations in adjacent domains (Figure 1). VSM measurements showed double hysteresis loops[21] of the EB system where the left loop possesses an EB field of $|\vec{H}_{EB,L}| = 28 \pm 1$ kA/m and a coercive field of $H_{C,L} = 5 \pm 1$ kA/m and the right loop an EB field of $|\vec{H}_{EB,R}| = 19 \pm 1$ kA/m and a coercive field of $H_{C,R} = 8 \pm 1$ kA/m.

The walls of the microfluidic chamber were fabricated from parafilm with an average height of 100 μm, and it was top-closed by a glass lid. The chamber's bottom area was square-shaped with a size of 1 cm^2 corresponding to a fluid container volume of 10 μL.

In the experiments spherical magnetic core−shell particles (Micromod GMBH) were used with a concentration of $c_P = 1.2 \times 10^8$ particles/mL in aqueous solution. The average particle diameter of $d_P = 2.00 \pm 0.02$ μm was determined by dynamic light scattering. The particles consisted of a styrene−maleic acid−copolymer matrix surrounded by superparamagnetic magnetite nanoparticles, encapsulated by a PEG-COOH polymer shell. The particles' average saturation magnetic moment of 4.48×10^{-14} Am^2 was determined from VSM measurements in an external magnetic field of 200 kA/m.

The microfluidic chamber was mounted on a sample stage centered between two air-cored solenoid pairs with their symmetry axes perpendicular and parallel to the sample surface plane (coordinate system see Figure 1). The current inducing the magnetic fields of the solenoids oscillated with trapezoidal (*TZ*) functions (Figure 2f), with a linear rise from $H_x = 0$ kA/m ($H_z =$ 0 kA/m) to $H_{x,max} = 0.32$ kA/m ($H_{z,max} = 1.6$ kA/m) within a rise time interval $\Delta t_{r,x}$ of 100 μs ($\Delta t_{r,z} = 500$ μs). For both directions the magnetic field alteration rate of $v_H = 3.2 \times 10^6$ (A/(m·s)) was the same. The same field alteration rate was chosen for decreasing the external magnetic fields resulting in fall time intervals from maximum fields to 0 of $\Delta t_{f,x} = 100$ μs ($\Delta t_{f,z} = 500$ μs). The field plateau time intervals $\Delta t_{p,x}$ ($\Delta t_{p,z}$) at $H_{x,max}$, ($H_{z,max}$) were chosen such that $\Delta t_{r,x} + \Delta t_{p,x} + \Delta t_{f,x} = \Delta t_{r,z} + \Delta t_{p,z} + \Delta t_{f,z} = \Delta t_{tot}$ and Δt_{tot} was varied between 200 and 800 ms. These two times correspond to frequencies of $\omega_{ext} = 2\pi/(2 \cdot \Delta t_{tot}) = 15.7$ and 3.9 Hz. The maximum magnetic field values used for the experiments were far below the required field for magnetization reversal. The oscillations of H_z advanced H_x by $\pi/2$, therefore $H_z(t) = H_{z,max} TZ(\omega_{ext} \cdot t)$ and $H_x(t) = H_{x,max} TZ(\omega_{ext} \cdot t - \pi/2)$.

Quantitative measurements of the particle transport were performed *via* an optical microscope set up equipped with a high-speed camera operating at a maximum frame rate of 2000 fps (Optronis CR450 ×2) and 40× optical magnification. The particle trajectories were subsequently analyzed by the software Videospottracker (CISMM).

Conflict of Interest: The authors declare no competing financial interest.

Supporting Information Available: A video demonstrating the magnetic particle transport. The Supporting Information is available free of charge on the ACS Publications website at DOI: 10.1021/acsnano.5b02283.

REFERENCES AND NOTES

1. Gijs, M. A. M. Magnetic Bead Handling on-Chip: New Opportunities for Analytical Applications. *Microfluid. Nanofluid.* **2004**, *1*, 22–40.
2. Jensen, K. F. Microreaction Engineering - Is Small Better? *Chem. Eng. Sci.* **2001**, *56*, 293–303.
3. Pamme, N. Magnetism and Microfluidics. *Lab Chip* **2006**, *6*, 24–38.
4. Neuberger, T.; Schöpf, B.; Hofmann, H.; Hofmann, M.; von Rechenberg, B. Superparamagnetic Nanoparticles for Biomedical Applications: Possibilities and Limitations of a New Drug Delivery System. *J. Magn. Magn. Mater.* **2005**, *293*, 483–496.
5. Won, J.; Kim, M.; Yi, Y.-W.; Kim, Y. H.; Jung, N.; Kim, T. K. A Magnetic Nanoprobe Technology for Detecting Molecular Interactions in Live Cells. *Science* **2005**, *309*, 121–125.
6. Holzinger, D.; Lengemann, D.; Göllner, F.; Engel, D.; Ehresmann, A. Controlled Movement of Superparamagnetic Bead Rows for Microfluid Mixing. *Appl. Phys. Lett.* **2012**, *100*, 153504.
7. Holzinger, D.; Ehresmann, A. Diffusion Enhancement in a Laminar Flow Liquid by near-Surface Transport of Superparamagnetic Bead Rows. *Microfluid. Nanofluid.* **2015**, 10.1007/s10404-015-1573-5.
8. Tierno, P.; Johansen, T. H.; Fischer, T. M. Magnetically Driven Colloidal Microstirrer. *J. Phys. Chem. B* **2007**, *111*, 3077–3080.
9. Ehresmann, A.; Lengemann, D.; Weis, T.; Albrecht, A.; Langfahl-Klabes, J.; Göllner, F.; Engel, D. Asymmetric Magnetization Reversal of Stripe-Patterned Exchange Bias Layer Systems for Controlled Magnetic Particle Transport. *Adv. Mater.* **2011**, *23*, 5568–5573.
10. Donolato, M.; Vavassori, P.; Gobbi, M.; Deryabina, M.; Hansen, M. F.; Metlushko, V.; Ilic, B.; Cantoni, M.; Petti, D.; Brivio, S.; et al. On-Chip Manipulation of Protein-Coated Magnetic Beads *via* Domain-Wall Conduits. *Adv. Mater.* **2010**, *22*, 2706–2710.
11. Chikazumi, S. *Physics of Ferromagnetism*; Oxford University Press: Oxford, 1997; pp 3−7.
12. Tierno, P.; Sagués, F.; Johansen, T. H.; Fischer, T. M. Colloidal Transport on Magnetic Garnet Films. *Phys. Chem. Chem. Phys.* **2009**, *11*, 9615–9625.
13. Yellen, B. B.; Erb, R. M.; Son, H. S.; Hewlin, R.; Shang, H.; Lee, G. U. Traveling Wave Magnetophoresis for High Resolution Chip Based Separations. *Lab Chip* **2007**, *7*, 1681–1688.
14. Donolato, M.; Dalslet, B. T.; Hansen, M. F. Microstripes for Transport and Separation of Magnetic Particles. *Biomicrofluidics* **2012**, *6*, 24110–241106.
15. Ahrend, F.; Holzinger, D.; Fohler, M.; Pofahl, S.; Wolff, U.; DeKieviet, M.; Schaefer, R.; Ehresmann, A. Stray Fields above Artificial Magnetic in-Plane Domains. *J. Magn. Magn. Mater.* **2015**, *381*, 292–296.
16. Lee, H.; Purdon, A. M.; Westervelt, R. M. Manipulation of Biological Cells Using a Microelectromagnet Matrix. *Appl. Phys. Lett.* **2004**, *85*, 1063–1065.
17. Yoon, M.; Kim, Y.; Kim, Y. M.; Yoon, H.; Volkov, V.; Avilov, A.; Park, Y. J.; Park, I. W. Superparamagnetism of Transition Metal Nanoparticles in Conducting Polymer Film. *J. Magn. Magn. Mater.* **2004**, *272−276*, e1259–e1261.
18. Potter, R. I. Analysis of Saturation Magnetic Recording Based on Arctangent Magnetization Transitions. *J. Appl. Phys.* **1970**, *41*, 1647.
19. Rugar, D.; Mamin, H. J.; Guethner, P.; Lambert, S. E.; Stern, J. E.; McFadyen, C.; Yogi, T. Magnetic Force Microscopy: General Principles and Application to Longitudinal Recording Media. *J. Appl. Phys.* **1990**, *68*, 1169–1183.
20. Liu, C.; Lagae, L.; Wirix-Speetjens, R.; Borghs, G. On-Chip Separation of Magnetic Particles with Different Magnetophoretic Mobilities. *J. Appl. Phys.* **2007**, *101*, 024913.
21. Holzinger, D.; Zingsem, N.; Koch, I.; Gaul, A.; Fohler, M.; Schmidt, C.; Ehresmann, A. Tailored Domain Wall Charges by Individually Set in-Plane Magnetic Domains for Magnetic Field Landscape Design. *J. Appl. Phys.* **2013**, *114*, 013908.
22. Mougin, A.; Poppe, S.; Fassbender, J.; Hillebrands, B.; Faini, G.; Ebels, U.; Jung, M.; Engel, D.; Ehresmann, A.; Schmoranzer, H. Magnetic Micropatterning of FeNi/FeMn Exchange Bias Bilayers by Ion Irradiation. *J. Appl. Phys.* **2001**, *89*, 6606–6608.
23. Fassbender, J.; Poppe, S.; Mewes, T.; Mougin, A.; Hillebrands, B.; Engel, D.; Jung, M.; Ehresmann, A.; Schmoranzer, H.; Faini, G.; et al. Magnetization Reversal of Exchange Bias Double Layers Magnetically Patterned by Ion Irradiation. *Phys. Stat. Sol. (A)* **2002**, *189*, 439–447.

24. Engel, D.; Kronenberger, A.; Jung, M.; Schmoranzer, H.; Ehresmann, A.; Paetzold, A.; Röll, K. Exchange Anisotropy Modification in NiO/NiFe Bilayers by Ion Bombardment. *J. Magn. Magn. Mater.* **2003**, *263*, 275–281.
25. Ehresmann, A.; Krug, I.; Kronenberger, A.; Ehlers, A.; Engel, D. In-Plane Magnetic Pattern Separation in NiFe/NiO and Co/NiO Exchange Biased Bilayers Investigated by Magnetic Force Microscopy. *J. Magn. Magn. Mater.* **2004**, *280*, 369–376.
26. Ehresmann, A. He-Ion Bombardment Induced Exchange Bias Modifications: Fundamentals and Applications. In *Recent Research Developments in Applied Physics Part II*; Pandalai, S. G., Ed.; Transworld Research Network: Kerala, 2004; Vol. 7, pp 401–421.
27. McCord, J.; Schäfer, R.; Theis-Bröhl, K.; Zabel, H.; Schmalhorst, J.; Höink, V.; Brückl, H.; Weis, T.; Engel, D.; Ehresmann, A. Domain Propagation in He-Ion-Bombarded Magnetic Wires with Opposite Exchange Bias. *J. Appl. Phys.* **2005**, *97*, 10K102.
28. Ehresmann, A.; Engel, D.; Weis, T.; Schindler, A.; Junk, D.; Schmalhorst, J.; Höink, V.; Sacher, M. D.; Reiss, G. Fundamentals for Magnetic Patterning by Ion Bombardment of Exchange Bias Layer Systems. *Phys. Status Solidi B* **2006**, *243*, 29–36.
29. Theis-Bröhl, K.; Wolff, M.; Westphalen, A.; Zabel, H.; McCord, J.; Höink, V.; Schmalhorst, J.; Reiss, G.; Weis, T.; Engel, D.; et al. Exchange-Bias Instability in a Bilayer with an Ion-Beam Imprinted Stripe Pattern of Ferromagnetic/antiferromagnetic Interfaces. *Phys. Rev. B: Condens. Matter Mater. Phys.* **2006**, *73*, 174408.
30. Lengemann, D.; Engel, D.; Ehresmann, A. Plasma Ion Source for *in situ* Ion Bombardment in a Soft X-Ray Magnetic Scattering Diffractometer. *Rev. Sci. Instrum.* **2012**, *83*, 053303.